RSC Advances

PAPER

View Article Online
View Journal | View Issue

Cite this: *RSC Adv.*, 2018, **8**, 27073

Flake-like $InVO_4$ modified TiO_2 nanofibers with longer carrier lifetimes for visible-light photocatalysts

Yun Zhou,[ab] Lixin Liu,[b] Tao Wu,[b] Guolong Yuan,[a] Junyu Li,[ab] Qiujie Ding,[ab] Fugang Qi,[a] Wenjun Zhu,[b] Xiaoping OuYang*[a] and Yuan Wang *[b]

Highly efficient solar light absorption capabilities and quantum yields in photocatalysts are key to their application in photocatalytic fields. Towards this end, TiO_2/$InVO_4$ nanofibers (NFs) have been designed and fabricated successfully by a one-pot electrospinning process. The resulting TiO_2/$InVO_4$ NFs display excellent visible-light photocatalytic activity, owing to their prominent visible-light absorption and electron–hole separation properties. Time-resolved transient PL spectroscopy demonstrated that the TiO_2/$InVO_4$ NFs display longer emission decay times (22.0 ns) compared with TiO_2 NFs (15.5 ns), implying that the heterojunction can remarkably suppress the electron–hole recombination and promote the carrier transfer efficiency. With tailored heterostructure features, TiO_2/$InVO_4$ NFs exhibit superior visible-light photodegradation activity, and after 80 min of visible-light irradiation, almost 95% of RhB molecules can be decomposed by TiO_2/$InVO_4$ NFs, while only 18% of RhB molecules can be decomposed by pure TiO_2 NFs.

Received 22nd May 2018
Accepted 23rd July 2018

DOI: 10.1039/c8ra04344b

rsc.li/rsc-advances

1. Introduction

Nowadays, with the overuse of various dyes and plastic products, organic pollutants in water and soil have drawn increasing attention. Among the various strategies, the development of efficient photocatalysts is a promising method for the treatment of organic pollutants, owing to its utilization of abundant solar energy, as well as its low cost and lack of secondary pollution during the course of decomposition.[1–3] Since A. Fujishima discovered the interesting phenomenon of light-induced water splitting by TiO_2 in the 1970s,[4] TiO_2 materials have been the most promising candidates for photocatalytic decontamination on account of their non-toxic, non-luminous corrosion, inert chemical properties, high photocatalytic activity, low cost, and cycle stability.[5–7] However, further application of TiO_2 photocatalysts is unfortunately limited by their large bandgap energy and short photogenerated carrier lifetimes.[8] To overcome these limitations, persistent research, such as non-metal element or metal ion doping,[9–11] surface modification,[12] semiconductor/metal combination,[13,14] and semiconductor/semiconductor hybridization,[15–17] has been engaged in order to narrow the bandgap energy for better visible-light absorption and promote electron–hole separation for longer carrier lifetimes. Herein, constructing a TiO_2-based semiconductor/semiconductor nanoheterostructured photocatalyst is an efficient method to increase visible-light harvesting and meanwhile suppress electron–hole recombination, ultimately leading to photocatalytic activity improvement.[18] Up until now, many TiO_2-based nanoheterostructures with excellent photocatalytic performance have been reported, such as TiO_2/SnO_2,[19] TiO_2/ZnO,[20] TiO_2/CdS,[21] TiO_2/MoS_2,[22] TiO_2/g-C_3N_4,[23] TiO_2/$CuInS_2$,[24] *etc.* Therefore, designing and constructing impactful nanoheterostructures is an effectual way to extend the lifetime of the photogenerated charge, and consequently improve the photocatalytic activity.

$InVO_4$ semiconductors, as an important group of semiconductors, have attracted much interest because of their potential applications in visible-light-driven photocatalysis, photoelectrochemistry, and gas sensing.[25,26] In particular, $InVO_4$ is considered to be an ideal choice for coupling with TiO_2 to improve the visible-light photocatalytic performance due to its relatively low bandgap energy ($E_g \approx 2.1$ eV) and energy level matching with TiO_2. Up till now, the process for fabricating TiO_2/$InVO_4$ NFs usually involves a few synthesis steps, including loading TiO_2 or $InVO_4$ particles on the surface of $InVO_4$ or TiO_2, such as *via* a hydrothermal method followed by an ion impregnate method.[27–29] Hence, the fabrication method for TiO_2/$InVO_4$ nanoheterostructures needs to be simplified. Furthermore, although previous research has revealed that TiO_2/$InVO_4$ heterostructures exhibit enhanced UV-Vis and visible-light photocatalytic performance, in-depth analysis of the charge transfer and carrier lifetimes of the nanoheterostructure is still missing. For example, Ge *et al.* explored

[a]School of Materials Science and Engineering, Xiangtan University, Xiangtan 411105, Hunan, China. E-mail: oyxp2003@alyun.com

[b]National Key Laboratory for Shock Wave and Detonation Physics, Institute of Fluid Physics, China Academy of Engineering Physics, P.O. Box 919-111, Mianyang, Sichuan 621900, People's Republic of China. E-mail: wangyuan0000@gmail.com

the visible-light photocatalytic performance of an $InVO_4$–TiO_2 photocatalyst synthesized by a sol–gel method, whereas further discussion on the photocatalytic improvement mechanism is absent.[30] Shen and Perales-Martínez proposed a mechanism for the electron–hole separation process in TiO_2/$InVO_4$ composites only based on the energy band structure, without intuitive experimental characterization.[27,28] Thus, it is necessary to further study the charge transfer and lifetime of the photogenerated charges of TiO_2/$InVO_4$ composites, and it should be clarified as to how much the heterojunction contributes to electron transport, and for how long the carrier lifetime can be obtained through separation at the interface of the heterojunction. Hence, the charge transfer mechanism and carrier lifetime of TiO_2/$InVO_4$ nanoheterostructures need to be analyzed in-depth.

In this paper, we successfully synthesized TiO_2/$InVO_4$ NFs by a one-pot electrospinning method for the first time, which could provide ample heterojunction interfaces as separation channels for photogenerated electron–hole pairs. Moreover, time-resolved transient PL spectroscopy was employed to confirm the carrier lifetime of the TiO_2/$InVO_4$ NFs. With the tailored nanoheterostructures, the prepared TiO_2/$InVO_4$ NFs exhibited enhanced photocatalytic activity due to broadened visible-light harvesting and efficiently prolonged carrier lifetimes resulting from the nanoheterojunction formed between TiO_2 and $InVO_4$.

2. Materials and methods

2.1 Synthesis of TiO_2/$InVO_4$ NFs

TiO_2/$InVO_4$ NFs were synthesized by a one-pot electrospinning process, as shown in Fig. 1(a). Briefly, 0.19 g $In(NO_3)_3 \cdot 4.5H_2O$, 0.18 g $VO(acac)_2$, 0.68 g tetrabutyl titanate (TBT), and 0.4 g polyvinylpyrrolidone (PVP) were added into a mixed solution of 2 g dimethylacetamide (DMAC), 1.0 ml ethanol, and 0.8 ml acetic acid, after which the above solution was magnetically stirred for 30 min, and thus an $In(NO_3)_3$/$VO(acac)_2$/TBT/PVP mixed solution with a Ti/In molar ratio of 4 : 1 was obtained. Then, the mixed solution was electrospun to compose the $In(NO_3)_3$/$VO(acac)_2$/TBT/PVP NFs. The electrospinning parameters were set as follows: 0.4 mm for the inner diameter of the spinneret, and 20 cm and 15 kV for the distance and DC voltage between the spinneret and the collector, respectively. Finally, the obtained NFs were annealed at 550 °C for 2 h in air to remove the PVP support and crystallise the TiO_2/$InVO_4$ NFs. A comparative sample of TiO_2 NFs was also synthesized by the same electrospinning method with a solution of 0.68 g tetrabutyl titanate (TBT) and 0.14 g polyvinylpyrrolidone (PVP) in a mixed solution of 1.0 ml ethanol and 0.8 ml acetic acid.

2.2 Photochemical experiments

The visible-light photocatalytic activity of the nanofibers was measured from the degradation of Rhodamine B (RhB)

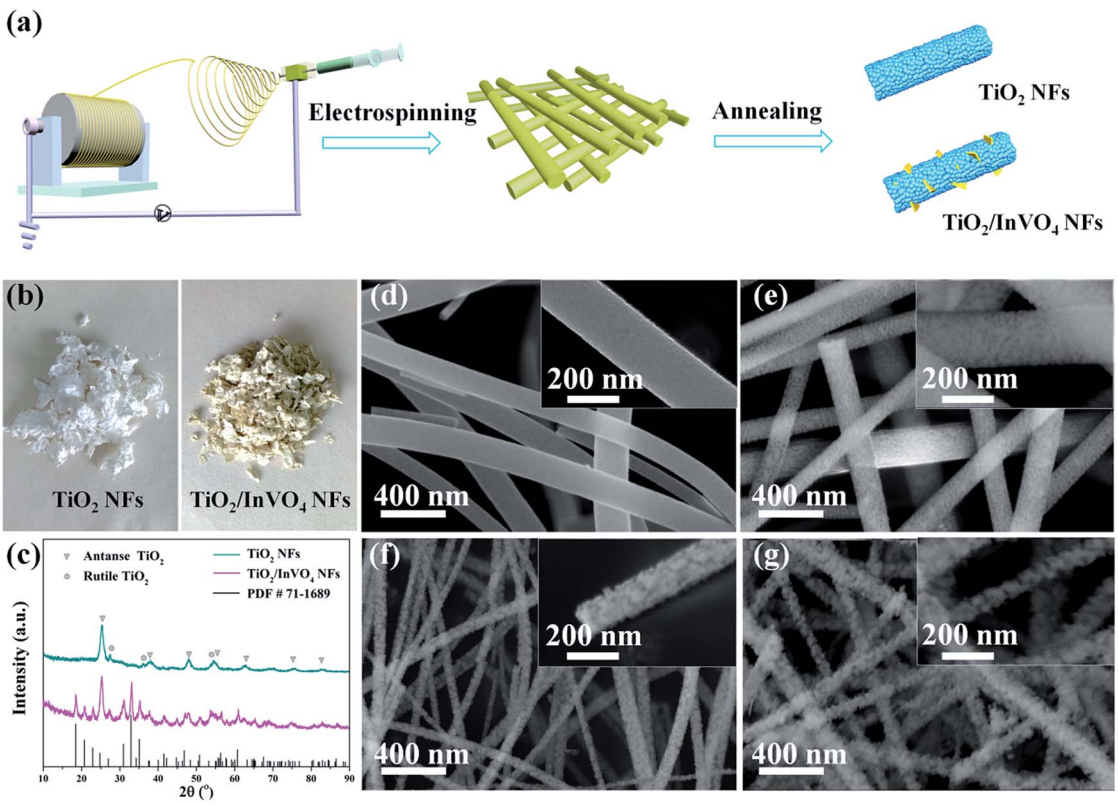

Fig. 1 (a) Schematic illustration of the fabrication process for the TiO_2 NFs and TiO_2/$InVO_4$ NFs. (b) Physical pictures and (c) XRD patterns of the TiO_2 NFs and TiO_2/$InVO_4$ NFs (Ti/In = 4 : 1). (d–g) SEM images of (d) the TiO_2 NFs and (e–g) TiO_2/$InVO_4$ NFs with Ti/In molar ratios of 8 : 1, 4 : 1, 2 : 1, respectively.

molecules. Firstly, 50 mg catalysts were added to 30 ml RhB (10 mg l^{-1}) solution and the suspensions were placed in dark environment for 30 min to reach an equilibrium of absorption and desorption. Secondly, a Xe lamp ($\lambda > 420$ nm) was employed for visible-light photocatalytic irradiation. At time intervals of 10 min, 3 ml suspensions were sucked and filtered to separate the catalysts. The variations in the filtrates were assessed using the change in the absorption band maximum recorded using a TU-1901 spectrophotometer.

2.3 Characterization

X-ray diffraction (XRD, X'pert Pro, CuKα, $\lambda = 1.5406$) and high-resolution transmission electron microscopy (HRTEM, Libra 200FE) were utilized to characterize the crystal structure of the nanofibers. Energy dispersive spectroscopy (EDS) and X-ray photoelectron spectroscopy (XPS) were employed to characterize the components of the samples. The morphologies of the nanofibers were obtained by Field emission scanning electron microscopy (FESEM, Hitachi S-4800) and TEM. Nitrogen adsorption–desorption isotherms (JW-BK122 W nitrogen adsorption apparatus) were used to evaluate the Brunauer–Emmett–Teller (BET) specific surface areas of the nanofibers. Furthermore, UV-Vis absorption spectra were obtained using a UV-3150 spectrophotometer, and photoluminescence (PL) spectra were obtained using a Raman spectrometer with a 532 nm laser excitation source. Transient PL curves for the nanofibers were recorded using a FLS920 fluorescence lifetime spectrophotometer (Edinburgh Instruments, UK) with the excitation wavelength at 532 nm.

3. Results and discussion

$TiO_2/InVO_4$ NFs were synthesized by a one-pot electrospinning process, as shown in Fig. 1(a). Physical pictures of the samples are displayed in Fig. 1(b). It is quite distinct that the color of the TiO_2 NFs is white, while the $TiO_2/InVO_4$ NFs appear to be faint yellow. Furthermore, XRD patterns are employed to characterize the phase composition of the resulting $TiO_2/InVO_4$ NFs, with the TiO_2 NFs as a reference sample, as presented in Fig. 1(c). The diffraction peaks of the TiO_2 NFs can be indexed to anatase TiO_2 (PDF #21-1272) and rutile TiO_2 (PDF #21-1276). In the case of the $TiO_2/InVO_4$ NFs, a superimposed XRD pattern of TiO_2 and orthorhombic $InVO_4$ (PDF #71-1689) is observed, which demonstrates both TiO_2 and $InVO_4$ with good crystallization in the $TiO_2/InVO_4$ NFs.

The general morphologies of the nanofibers are obtained from SEM images and the results are demonstrated in Fig. 1(d), in which it is clearly revealed that one-dimensional TiO_2 and $TiO_2/InVO_4$ structures have been successfully constructed. As shown in Fig. 1(d), the TiO_2 NFs have rough and uniform morphologies, with average diameters of about 150 nm and lengths of about a few micrometers. The morphologies of the $TiO_2/InVO_4$ NFs with different Ti/In molar ratios are presented in Fig. 1(e–g), which all have an average length of a few micrometers, as well as loose and rough surfaces. Furthermore, with a decrease in the Ti/In molar ratio, it is obvious that the average diameter of the $TiO_2/InVO_4$ NFs decreases and the surface of the $TiO_2/InVO_4$ NFs becomes much more loose and rough, which can be attributed to the adjustment of the PVP amount and the epitaxial growth of $InVO_4$ in the electrospinning process.

To further confirm the microscopic morphologies and crystal structures of the $TiO_2/InVO_4$ NFs, TEM images are recorded in Fig. 2. It is obvious that the $TiO_2/InVO_4$ NFs with a diameter of ~100 nm (Fig. 2(a)) are composed of many distinct crystal particles and flakes, as displayed in Fig. 2(b). Then, we obtained an HRTEM image of the $TiO_2/InVO_4$ NFs to further observe the distributional crystal particles, and the result is presented in Fig. 2(c). The lattice distance of 0.35 nm is attributed to the (101) lattice distance of anatase TiO_2, and the measured lattice fringes of 0.28 nm and 0.36 nm correspond to the interplanar spacings of the (200) and (021) planes of orthorhombic $InVO_4$, respectively, indicating that the $TiO_2/InVO_4$ nanoheterostructures have been prepared successfully. Additionally, the results of the STEM-EDS elemental mapping analysis are displayed in Fig. 2(d–g) to further explore the element distributions in the $TiO_2/InVO_4$ nanofibers. It is obvious that the $TiO_2/InVO_4$ nanofibers are mainly composed of the metals Ti, In, and V, and the diameters of In and V are larger than that of Ti, which indicates that the flake-structure on the surfaces of the $TiO_2/InVO_4$ NFs can be assigned to the secondary growth of $InVO_4$.

In order to further determine the molar ratio of elements in all the $TiO_2/InVO_4$ NFs (Ti/In = 4 : 1), energy dispersive spectroscopic (EDS) analysis was applied and the results are shown in Fig. 3, in which it can be observed that Ti, In, V, and O appear in the $TiO_2/InVO_4$ NFs, and the atomic ratios of Ti, In, and V are

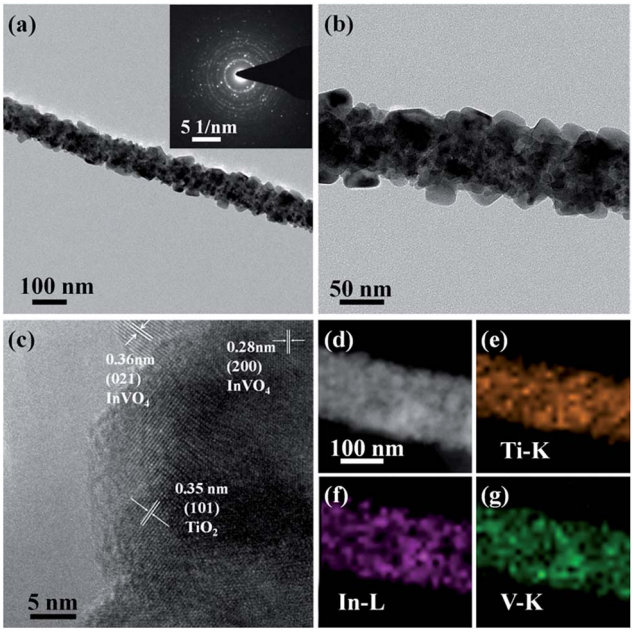

Fig. 2 (a and b) TEM images and (c) a high magnification TEM (HRTEM) image of the $TiO_2/InVO_4$ NFs (Ti/In = 4 : 1); (d–g) STEM image of the $TiO_2/InVO_4$ NFs (Ti/In = 4 : 1) (d), and the corresponding EDX elemental maps of Ti (e), In (f), and V (g), respectively.

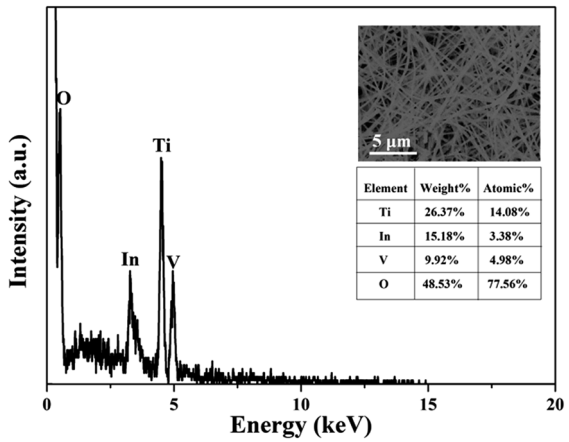

Fig. 3 EDS pattern of the $TiO_2/InVO_4$ NFs (Ti/In = 4 : 1).

14.08%, 3.38%, and 4.98%, respectively, implying the molar ratio of Ti/In is about 4.2, which is in agreement with the set value of the Ti/In molar ratio in the electrospinning process. Furthermore, XPS measurements were employed and the results are displayed in Fig. 4. Fig. 4(a) shows the holistic survey spectrum of the $TiO_2/InVO_4$ NFs, in which Ti, In, V, and O are detected. In addition, the Ti 2p, In 3d, and V 2p core-level spectra of the $TiO_2/InVO_4$ NFs are shown in Fig. 4(b–d). The peaks at 444.5 eV and 452.0 eV in the In 3d core-level spectrum, as shown in Fig. 3(b), correspond to In 3d3/2 and In 3d5/2 for In^{3+} species, respectively.[31] As shown in Fig. 4(c), the V 2p peaks are located at 517.1 eV and 524.6 eV, which can be ascribed to V^{5+}.[32] From the Ti 2p core-level spectrum in Fig. 4(d), two clearly evident peaks centered at 463.8 and 458.2 eV can be assigned to Ti 2p1/2 and Ti 2p3/2, respectively, which belong to the Ti^{4+} elemental chemical state of TiO_2.[33] It can be therefore concluded that the $TiO_2/InVO_4$ NFs have been fabricated successfully.

We then investigated the photocatalytic performance of TiO_2 NFs and $TiO_2/InVO_4$ NFs with different Ti/In molar ratios

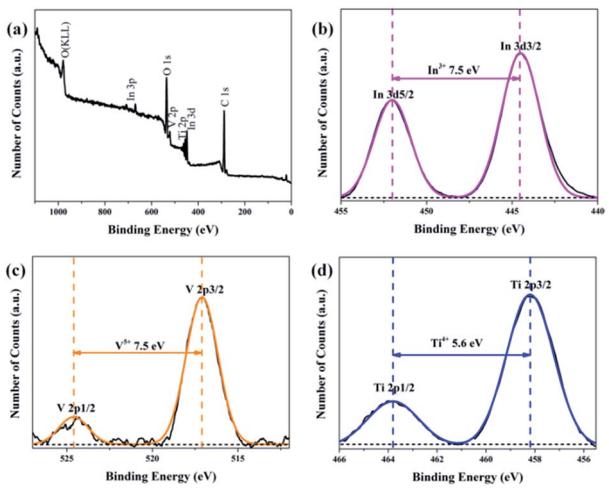

Fig. 4 (a) XPS survey spectrum of the $TiO_2/InVO_4$ NFs (Ti/In = 4 : 1), and (b–d) high resolution XPS spectra of the In 3d, V 2p, and Ti 2p core-level binding energies, respectively.

toward the photodegradation process of RhB solution. As shown in Fig. 5(a), after adding 50 mg $TiO_2/InVO_4$ NFs (Ti/In = 4 : 1) as a photocatalyst into RhB solution, the λ_{max} intensity of the absorption spectral changes of the RhB solution is significantly decreased with irradiation time. Fig. 5(b) presents the corresponding concentration change in the RhB solution when using different samples as photocatalysts under visible-light irradiation. It is obviously that after 80 min of visible-light irradiation, only 18% and 32% of RhB molecules are decomposed by the TiO_2 NFs and standard P25, respectively, which can be assigned to their poor visible-light absorption and short photogenerated charge lifetime. As for the $TiO_2/InVO_4$ NFs, at least 80% of RhB molecules are effectively decomposed, indicating that the $TiO_2/InVO_4$ NFs achieve an outstanding enhanced visible photocatalytic performance, better than that of pure TiO_2 NFs. Moreover, while using the $TiO_2/InVO_4$ NFs with a Ti/In molar ratio of 4 : 1 as photocatalysts, about 95% of RhB molecules are decomposed. In addition, as shown in Fig. 5(c), the degradation rates obtained over the $TiO_2/InVO_4$ NFs (Ti/In = 4 : 1), $TiO_2/InVO_4$ NFs (Ti/In = 2 : 1), $TiO_2/InVO_4$ NFs (Ti/In = 8 : 1), P25, and TiO_2 NFs are 0.03632, 0.0238, 0.01756, 0.0033, and 0.00244, respectively. Furthermore, the photocatalytic performance of $TiO_2/InVO_4$ NFs was enhanced with the increasing amount of $InVO_4$ and reached the best photocatalytic activity at a Ti/In molar ratio of 4 : 1. The increasing surface area with the increase in the amount of $InVO_4$ is beneficial for the improvement of the photocatalytic activity, which is in agreement with the morphology results and dark absorption during the photocatalysis process. However, with a further increase of $InVO_4$ amount, the epitaxial growth of $InVO_4$ would undermine the uniformity of the nano-heterostructures and suppress the separation of the electron–hole pairs, so superabundant $InVO_4$ is conversely unfavorable for improving photocatalytic activity. So, the $TiO_2/InVO_4$ NFs

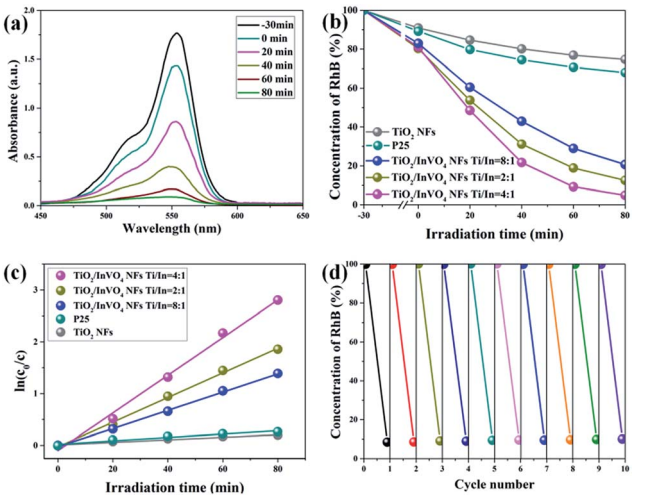

Fig. 5 (a) Absorption spectral changes of RhB solution in the presence of $TiO_2/InVO_4$ NFs (Ti/In = 4 : 1) under visible-light irradiation. (b) Comparison of the visible-light photocatalytic degradation of RhB and (c) the photodegradation rates in the presence of TiO_2 and $TiO_2/InVO_4$ NFs. (d) Cycling tests of the photocatalytic activity of the $TiO_2/InVO_4$ NFs (Ti/In = 4 : 1).

with a Ti/In molar ratio of 4 : 1 may exhibit outstanding synergistic effects with an appropriate surface area and nanoheterostructure, thereby allowing them to displaying the highest photocatalytic activity. Hence, we mainly conducted in-depth causal discussions on the enhanced visible-light photocatalytic performance of TiO_2/$InVO_4$ NFs with a Ti/In molar ratio of 4 : 1 in the following research. Based on further practical application, the stability of the photocatalyst is a very significant factor for recycling. Herein, ten cycles of the photodegradation behaviour of RhB are shown in Fig. 5(d) in order to evaluate the photocatalytic stability of the TiO_2/$InVO_4$ NFs. After each cycle of the photocatalysis reaction process, it can seen that there is only negligible reduction in the photocatalytic activity, indicating the excellent reusability and stability of the TiO_2/$InVO_4$ NFs. In a word, TiO_2/$InVO_4$ NFs exert an outstanding stability, and a much enhanced visible-light photocatalytic activity compared with pure TiO_2 NFs.

Based on the excellent results, we have mainly conducted in-depth causal discussions on three aspects of the enhanced visible-light photocatalytic performance of the TiO_2/$InVO_4$ NFs. Firstly, it is well known that surface area is an important factor for photocatalysis.[34] Hence, as shown in Fig. 6(a), we employed a BET adsorption/desorption of nitrogen gas method to evaluate the specific surface area of the TiO_2 NFs and TiO_2/$InVO_4$ NFs. The BET surface area of the TiO_2/$InVO_4$ NFs, calculated from the nitrogen isotherm curve, is 30.5 $m^2\ g^{-1}$, which is about two times higher than that of the TiO_2 NFs (16.8 $m^2\ g^{-1}$). Obviously, the increased surface area of the TiO_2/$InVO_4$ NFs would provide a larger available active area for the photocatalytic reaction. Accordingly, the increasing surface area of the TiO_2/$InVO_4$ NFs would efficiently promote photocatalytic activity.

In particular, optical absorption characteristics have a direct influence on the photocatalytic activity of semiconductors. Herein, we employed UV-Vis absorbance spectroscopy to attest whether TiO_2/$InVO_4$ NFs have a wider light absorption range for visible light compared with TiO_2 NFs, and the results are shown in Fig. 6(b). TiO_2 NFs present an evident absorption edge located at 400 nm, derived from the intrinsic energy gap of TiO_2. The UV-Vis spectra of the TiO_2/$InVO_4$ NFs reveal a wide visible-light absorption band around 400–650 nm, which contributed to the introduction of the narrow band gap $InVO_4$ semiconductor. This effectual change of the absorption spectra indicates that the TiO_2/$InVO_4$ NFs have broader spectral harvesting, ultimately leading to the improvement of the visible-light photocatalytic activity.

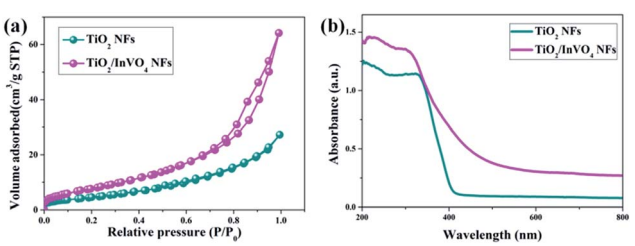

Fig. 6 (a) N_2 adsorption–desorption isotherms and (b) UV-Vis absorbance spectra of the TiO_2 NFs and TiO_2/$InVO_4$ NFs.

It is fairly well acknowledged that a lower PL emission intensity of the samples under the same laser irradiation intensity implies less electron–hole recombination.[35] Herein, we employed steady-state and time-resolved transient PL spectroscopy to characterize the capability of electron–hole pair separation in the nanofibers. As shown in Fig. 7(a), in the TiO_2 NF PL spectrum, the strong emission band at around 550–850 nm is mainly attributed to deep and shallow trap centers of oxygen defects and excitons.[36] However, the TiO_2/$InVO_4$ NFs have a substantially lower PL intensity than the TiO_2 NFs, which implies that recombination of the photogenerated electron–hole pairs in the TiO_2/$InVO_4$ NFs is effectively suppressed.

Time-resolved photoluminescence (TRPL) is an effective method employed to extract the carrier lifetime (τ), which can directly indicate various radiative and non-radiative loss channels responsible for photogenerated carrier recombination.[37] To further verify the nanoheterojunction's functions of electron–hole separation and carrier transfer in the TiO_2/$InVO_4$ NFs, TRPL was employed at room temperature to explore the dynamics of the photogenerated charge. The transient emission spectra for the TiO_2 NFs and TiO_2/$InVO_4$ NFs are shown in Fig. 7(b and c). The PL decay profile is fitted using a multi-exponential function as follows:[38,39]

$$I_t = \sum_{i=1}^{n} A_i \exp(-t/\tau_i) \quad (1)$$

where I_t is intensity, A_i is the relative magnitude of the ith decay, and τ_i is the ith decay time. It can be deduced that the TiO_2/$InVO_4$ NFs yield the longest decay time (τ_1 = 2.047 ns, A_1 = 0.1475; τ_2 = 27.862 ns, A_2 = 0.0368) compared with the TiO_2 NFs (τ_1 = 1.339 ns, A_1 = 0.2172; τ_2 = 23.686 ns, A_2 = 0.212). Furthermore, the fast factor (τ_1) commonly corresponds to the non-radiative relaxation process, owing to oxide defects,[40] and the slow factor (τ_2) is attributed to the radiative pathway, related to the recombination of photogenerated electron–hole pairs.[41] Furthermore, the average lifetimes (τ_{ave}) can be deduced through the following equation for a general comparison of the carrier lifetime:[42]

$$\tau_{ave} = f_1\tau_1 + f_2\tau = \frac{A_1\tau_2^2 + A_2\tau_2^2}{A_1\tau_1 + A_2\tau_2} \quad (2)$$

The values for the average time calculated based on two-exponential decays for the TiO_2/$InVO_4$ NFs and TiO_2 NFs are 22 ns and 15 ns, respectively. In order to compare the separation efficiency of the TiO_2/$InVO_4$ heterostructures, we list the carrier lifetimes of different TiO_2-based heterostructures reported previously in Table 1, and it is obvious that the TiO_2/$InVO_4$ NFs with tailored heterostructure features exhibit longer carrier lifetimes than TiO_2/SiO_2, TiO_2/In_2S_3, and TiO_2/MoS_2, implying that this kind of heterostructure prepared by electrospinning can provide ample heterojunction interfaces for more separation channels for photogenerated electron–hole pairs.

To better understand the charge separation in TiO_2/$InVO_4$ NFs, a schematic illustration of the efficient separation and

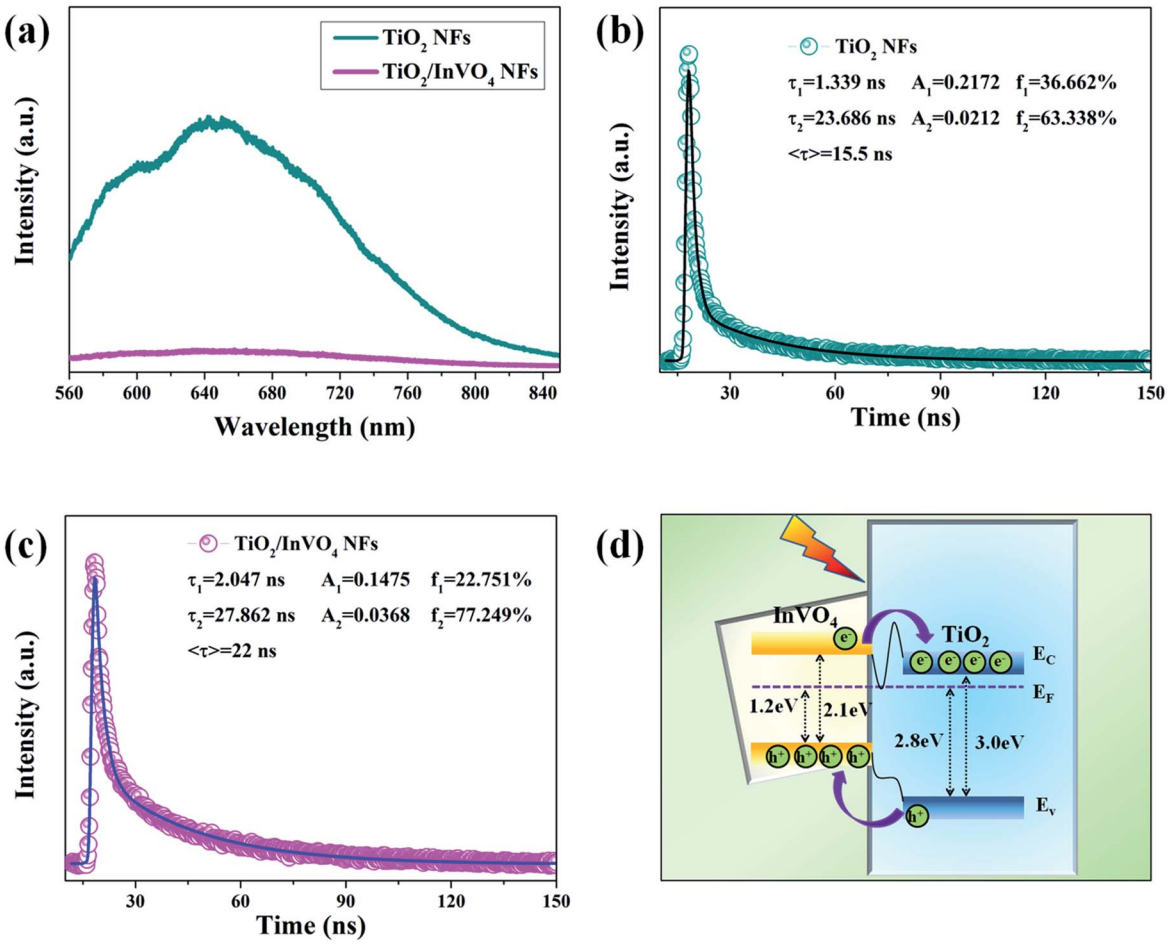

Fig. 7 (a) Steady-state PL spectra of TiO_2 NFs and TiO_2/$InVO_4$ NFs (Ti/In = 4 : 1). (b and c) Time-resolved transient PL decay of TiO_2 NFs and TiO_2/$InVO_4$ NFs (Ti/In = 4 : 1), respectively. (d) Schematic illustration of energy band matching and the proposed mechanism of charge carrier transition for TiO_2/$InVO_4$ nanoheterojunctions under visible-light irradiation, including conduction bands (E_C), valence bands (E_V), and Fermi levels (E_F).

transport of photogenerated charge in the TiO_2/$InVO_4$ NFs is represented in Fig. 7(d). The standard literature energy levels of TiO_2 and $InVO_4$ (conduction bands of −4.0 eV and −3.6 eV, valance bands of −7.0 eV and −5.7 eV, and Fermi levels of −4.2 eV and −4.5 eV, *vs.* the vacuum level, respectively) were employed for the energy band matching analysis here.[45] The matching energy band between $InVO_4$ and TiO_2 is shown in Fig. 6(d), when the nanoheterostructures are formed, the Fermi energy bands of TiO_2 and $InVO_4$ are at the same level, which thus leads both the conduction band (E_C) and valence band (E_V) of $InVO_4$ to locate above those of TiO_2. Under visible-light irradiation, $InVO_4$ in the TiO_2/$InVO_4$ NFs is photoexcited to produce electron–hole pairs, and owing to the incomparable nanoheterojunction structure formed at the interfaces of TiO_2 and $InVO_4$, the photogenerated electrons can facilely transport to the E_C of TiO_2. Hereby, numerous photogenerated electrons transport from the E_C of $InVO_4$ to that of TiO_2, and photogenerated holes concentrate on the E_V of $InVO_4$. In this way, the separation of the photogenerated charge can be efficiently facilitated, thereby prolonging the carrier lifetimes and resulting in the enhanced photocatalytic activity of the TiO_2/$InVO_4$ NFs under visible-light irradiation.

Table 1 Carrier lifetimes of different TiO_2-based heterostructures

Heterostructure composites	TiO_2/$InVO_4$ NFs	TiO_2/SiO_2 film[43]	TiO_2/In_2S_3 nanobelts[40]	TiO_2/MoS_2 nanocomposite[44]
τ_1 (ns)	2.047	0.0824	0.67	—
τ_2 (ns)	27.862	0.898	4.64	—
T_{ave} (ns)	22	—	—	9.49

4. Conclusions

In summary, TiO_2/$InVO_4$ NFs were successfully fabricated by a facile one-pot electrospinning method. The TiO_2/$InVO_4$ NFs showed a significantly enhanced photocatalytic performance; almost 95% of RhB molecules were decomposed within 80 min by the TiO_2/$InVO_4$ NFs (Ti/In = 4 : 1), but only 18% of RhB molecules were decomposed by pure TiO_2 NFs. Moreover, the time-resolved transient PL spectra reveal that the TiO_2/$InVO_4$ NFs exhibit a prolonged average carrier lifetime of 22 ns, more

than that of the TiO_2 NFs, which can promote photogenerated carrier separation. Accordingly, the resulting $TiO_2/InVO_4$ NFs display excellent visible-light photocatalytic performance, owing to their prominent visible-light harvesting and electron–hole separation properties. It is indisputable that $TiO_2/InVO_4$ NFs may shed new light on highly efficient visible-light nano-heterostructured photocatalysts with longer carrier lifetimes.

Conflicts of interest

There are no conflicts to declare.

Acknowledgements

This work was supported by the National Natural Science Foundation of China (No. 11704354) and the Hunan Provincial Innovation Foundation for Postgraduate (No. 8443|431000203431000203).

Notes and references

1 D. M. Schultz and T. P. Yoon, *Science*, 2014, **343**, 1239176.
2 K. Nakata, B. Liu, Y. Goto, T. Ochiai, M. Sakai, H. Sakai, T. Murakami, M. Abe and A. Fujishima, *Chem. Lett.*, 2011, **40**, 1161–1162.
3 J. Ran, J. Zhang, J. Yu, M. Jaroniec and S. Z. Qiao, *Chem. Soc. Rev.*, 2014, **43**, 7787–7812.
4 A. Fujishima and K. Honda, *Nature*, 1972, **238**, 37.
5 Y. Bai, I. Mora-Sero, F. D. Angelis, J. Bisquert and P. Wang, *Chem. Rev.*, 2014, **114**, 10095–10130.
6 S. G. Kumar and L. G. Devi, *J. Phys. Chem. A*, 2011, **115**, 13211–13241.
7 C. P. Sajan, S. Wageh, A. A. Al-Ghamdi, J. Yu and S. Cao, *Nano Res.*, 2016, **9**, 3–27.
8 J. Hensel, G. Wang, Y. Li and J. Z. Zhang, *Nano Lett.*, 2010, **10**, 478–483.
9 R. Asahi, T. Morikawa, T. Ohwaki, K. Aoki and Y. Taga, *Science*, 2001, **293**, 269–271.
10 T. Huang, S. Mao, J. Yu, Z. Wen, G. Lu and J. Chen, *RSC Adv.*, 2013, **3**, 16657–16664.
11 W. He, Z. Fang, K. Zhang, X. Li, D. Ji, X. Jiang, C. Qiu and K. Guo, *RSC Adv.*, 2015, **5**, 54853–54860.
12 X. Chen, L. Liu, Y. Y. Peter and S. S. Mao, *Science*, 2011, **331**, 746–750.
13 Y. Shi, D. Yang, Y. Li, J. Qu and Z. Z. Yu, *Appl. Surf. Sci.*, 2017, **426**, 622–629.
14 X. Zhang, Z. Shen, C. Cheng, L. Shi, R. Cheng and J. Dong, *RSC Adv.*, 2017, **7**, 52172–52179.
15 C. Cheng, J. Shi, Y. Hu and L. Guo, *Nanotechnology*, 2017, **28**, 164002.
16 H. Zhang, F. Liu, H. Wu, X. Cao, J. Sun and W. Lei, *RSC Adv.*, 2017, **7**, 40327–40333.
17 M. N. Ha, F. Zhu, Z. Liu, L. Wang, L. Liu, G. Lu and Z. Zhao, *RSC Adv.*, 2016, **6**, 21111–21118.
18 H. Wang, L. Zhang, Z. Chen, J. Hu, S. Li, Z. Wang, J. Liu and X. Wang, *Chem. Soc. Rev.*, 2014, **43**, 5234–5244.
19 C. Cheng, W. Ren and H. Zhang, *Nano Energy*, 2014, **5**, 132–138.
20 P. G. Ramos, E. Flores, L. A. Sánchez, R. J. Candal, M. Hojamberdiev, W. Estrada and J. Rodriguez, *Appl. Surf. Sci.*, 2017, **426**, 844–851.
21 F. Tian, D. Hou, F. Hu, K. Xie, X. Qiao and D. Li, *Appl. Surf. Sci.*, 2017, **391**(Part B), 295–302.
22 X. Ren, X. Qi, Y. Shen, S. Xiao, G. Xu, Z. Zhang, Z. Huang and J. Zhong, *J. Phys. D: Appl. Phys.*, 2016, **49**, 315304.
23 S. P. Adhikari, G. P. Awasthi, J. Lee, C. H. Park and C. S. Kim, *RSC Adv.*, 2016, **6**, 55079–55091.
24 F. Xu, J. Zhang, B. Zhu, J. Yu and J. Xu, *Appl. Catal., B*, 2018, **230**, 194–202.
25 X. Zhang, *Catal. Lett.*, 2014, **144**, 1253–1257.
26 Y. Yan, X. Liu, W. Fan, P. Lv and W. Shi, *Chem. Eng. J.*, 2012, **200–202**, 310–316.
27 J. Shen, H. Yang, Y. Feng, Q. Cai and Q. Shen, *Solid State Sci.*, 2014, **32**, 8–12.
28 I. A. Perales-Martínez, V. Rodríguez-González, S. W. Lee and S. Obregón, *J. Photochem. Photobiol., A*, 2015, **299**, 152–158.
29 Y. Min, K. Zhang, Y. C. Chen and Y. G. Zhang, *Ultrason. Sonochem.*, 2012, **19**, 883–889.
30 L. Ge, M. Xu and H. Fang, *Mater. Lett.*, 2007, **61**, 63–66.
31 F. Guo, W. Shi, X. Lin, X. Yan, Y. Guo and G. Che, *Sep. Purif. Technol.*, 2015, **141**, 246–255.
32 A. Chakrabarti, K. Hermann, R. Druzinic, M. Witko, F. Wagner and M. Petersen, *Phys. Rev. B: Condens. Matter Mater. Phys.*, 1999, **59**, 10583–10590.
33 H. Li, Y. Wang, G. Chen, Y. Sang, H. Jiang, J. He, X. Li and H. Liu, *Nanoscale*, 2016, **8**, 6101–6109.
34 G. Tian, Y. Chen, W. Zhou, K. Pan, C. Tian, X. Huang and H. Fu, *CrystEngComm*, 2011, **13**, 2994.
35 Z. Zhang, C. Shao, X. Li, L. Zhang, H. Xue, C. Wang and Y. Liu, *J. Phys. Chem. C*, 2010, **114**, 7920–7925.
36 K. Iijima, M. Goto, S. Enomoto, H. Kunugita, K. Ema, M. Tsukamoto, N. Ichikawa and H. Sakama, *J. Lumin.*, 2008, **128**, 911–913.
37 H. H. Wang, Q. Chen, H. Zhou, L. Song, Z. S. Louis, N. D. Marco, Y. Fang, P. Sun, T. B. Song, H. Chen and Y. Yang, *J. Mater. Chem. A*, 2015, **3**, 9108–9115.
38 J. L. Wu, F. C. Chen, Y. S. Hsiao, F. C. Chien, P. L. Chen, C. H. Kuo, M. H. Huang and C. S. Hsu, *ACS Nano*, 2011, **5**, 959–967.
39 S. W. Cao, X. F. Liu, Y. P. Yuan, Z. Y. Zhang, Y. S. Liao, J. Fang, S. C. J. Loo, T. C. Sum and C. Xue, *Appl. Catal., B*, 2014, **147**, 940–946.
40 Y. Li, T. Li, J. Tian, X. Wang and H. Cui, *Part. Part. Syst. Charact.*, 2017, **34**, 1700127.
41 X. Zeng and W. Qin, *Mater. Lett.*, 2016, **182**, 347.
42 B. R. Masters, *J. Biomed. Opt.*, 2008, **13**, 029901.
43 K. Miyashita, S. Kuroda, S. Tajima, K. Takehira, S. Tobita and H. Kubota, *Chem. Phys. Lett.*, 2003, **369**, 225–231.
44 H. S. Han, K. M. Kim, C. W. Lee, C. S. Lee, R. C. Pawar, J. L. Jones, Y. R. Hong, J. H. Ryu, T. Song, S. H. Kang, H. Choi and S. Mhin, *Phys. Chem. Chem. Phys.*, 2017, **19**, 28207–28215.
45 G. Xiao, X. Wang, D. Li and X. Fu, *J. Photochem. Photobiol., A*, 2008, **193**, 213–221.